Quattroped: A Leg–Wheel Transformable Robot

Shen-Chiang Chen, Ke-Jung Huang, Wei-Hsi Chen, Shuan-Yu Shen, Cheng-Hsin Li, and Pei-Chun Lin, *Member, IEEE*

***Abstract*—This paper reports on the design, integration, and performance evaluation of a novel four-leg/four-wheel transformable mobile robot, *Quattroped*. In contrast to most hybrid platforms that have separate mechanisms and actuators for wheels and legs, this robot is implemented with a unique transformation mechanism that directly switches the morphology of the driving mechanism between the wheels (i.e., a full circle) and 2 degrees of freedom leg (i.e., combining two half circles as a leg), so that the same system of actuation power can be efficiently utilized in both wheeled and legged modes. The design process, mechatronics, software infrastructure, behavioral development, and leg–wheel dynamic characteristics are described. The performance of the robot is evaluated in various scenarios, including driving and turning in wheeled mode, driving, step and bar crossing, irregular terrain passing, and stair climbing in legged mode. Taking advantage of the leg–wheel combination on a single platform, the comparison of the wheeled and legged locomotion is also discussed.**

***Index Terms*—Leg, locomotion, mobile robot, transformable, wheel.**

I. Introduction

LEGS and wheels are two widely adopted methodologies utilized by ground locomotion platforms. After a long evolution, legs appeared on most ground animals, and these agile and robust legs became capable of allowing animals to move smoothly and rapidly over uneven terrain. With the appearance of various advanced mechatronic components, building bioinspired robots becomes feasible [1], [2], and legged robotics has recently received significant attention [3]–[5]. Wheels, on the other hand, are human inventions specialized for locomotion on flat ground; their excellent performance, efficiency, and smooth traveling at a high speed on flat ground sets a standard that can hardly be bested by legged locomotion. Thus, a leg–wheel hybrid platform with great mobility on both flat ground (via wheels) and rough terrain (with legs) seems to be an adequate combination of a mobile platform suitable for general indoor–outdoor and flat–rough environments.

Leg–wheel hybrid mobile platforms can generally be categorized according to their morphology [6]. Popular categories include "articulated-wheeled" robots, where the robots usually combine active or passive wheels on the feet of the articulated legs. For example, the quadruped Roller Walker has passive wheels on the feet of 3-degree-of-freedom (DOF) legs, so its locomotion can be switched from walking to roller skating on flat ground [7]. The quadruped Paw [8], by having four active wheels on the distal ends of its compliant legs, has better mobility on flat ground. The robot Octal Wheel has a special wheel–arm mechanism that is composed of an arm with two wheels mounted on each side, and the robot is capable of climbing over obstacles such as stairs [9]. A similar mechanism is adopted by the robot HANZO as well [10]. Loper climbs stairs by rotating four Tri-lobe wheels [11]. The robots Epi.q-1 and Epi.q-2 have three wheels mounted on the rotatable and retractable wheel–arm mechanism on each leg–wheel, thereby increasing the ability for rough terrain negotiation [12]. Shrimp Rover has a special mechanism design that combines wheels and self-adjustable linkages to maintain a suitable body posture and increase its mobility over stairs and uneven terrain [13]. Similar strategy can also be found in Hylos [14].

Another popular category is "leg–wheel separated" robots, where the robots have both legs and wheels mounted on the body, and its motion is generated by collaboration of these two mechanisms. For example, Chariot III has two big wheels and four 3-DOF legs [15]. Wheeleg has two pneumatically actuated 3-DOF front legs and two independently driven rear wheels [16]. Other morphologies are also proposed by researchers. For example, Whegs has four 3-spoke wheels without rims, and it performs well on both flat and rough terrain [17]. Impass has similar "rimless" wheels, whose spokes can actively change their lengths to maintain posture and stability while climbing obstacles [18]. The hexapod RHex with 1 active rotational DOF on each half-circle leg can easily generate various legged behaviors via open-loop control [19]. The planar robot Rolling Disk Biped (RDB) can walk and roll by overall morphology change [20]. A similar morphology is utilized as the leg–wheel module on a hybrid robot [21]. PEOPLER-II has two bars mounted on each of the four wheels, and locomotion can be switched between leg type and wheel type [22]. In addition, some robots utilize tracks [23] or hybridize them with the legs or wheels to generate robust locomotion on rough ground, for example, Azimut [6].

Here, we adopt a different methodology and design a four-leg/four-wheel transformable mobile robot, *Quattroped*, as shown in Fig. 1. The robot is neither "articulated-wheeled" nor

Manuscript received March 28, 2012; revised September 19, 2012 and January 17, 2013; accepted February 21, 2013. Date of publication April 25, 2013; date of current version February 20, 2014. Recommended by Technical Editor M. de Queiroz. This work was supported by the National Science Council (NSC), Taiwan, under Contract NSC 97-2218-E-002-022-MY3 and 100-2628-E-002-021-MY3. This paper was presented in part at the IEEE/RSJ International Conference on Intelligent Robots and Systems, St. Louis, MO, USA, October 2009, and in part at the 2011 IEEE International Conference on Robotics and Automation, Shanghai, China, May 2011.

The authors are with the Department of Mechanical Engineering, National Taiwan University, Taipei 106, Taiwan (e-mail: ohjoechen@hotmail.com; b95502111@ntu.edu.tw; weinitor@gmail.com; shanueshen@yahoo.com.tw; minnelee@hotmail.com; peichunlin@ntu.edu.tw).

This paper has supplementary downloadable material available at http://ieeexplore.ieee.org, provided by the authors. The material includes eight videos in .mpg format showing the robot *Quattroped* operated in various scenarios. Total size is 16.2 MB. Contact peichunlin@ntu.edu.tw for further questions about this work.

Color versions of one or more of the figures in this paper are available online at http://ieeexplore.ieee.org.

Digital Object Identifier 10.1109/TMECH.2013.2253615

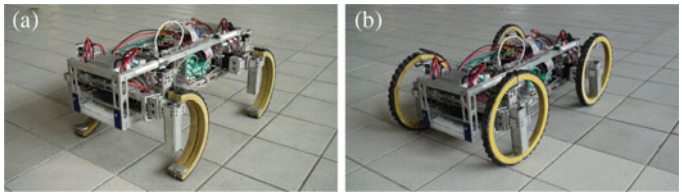

Fig. 1. Leg–wheel transformable robot, *Quattroped*: (a) legged mode and (b) wheeled mode.

"leg–wheel separated," but is equipped with a "transformation mechanism" capable of directly switching the morphology of a wheel (i.e., a full circle) into a leg (i.e., combining two half circles as a leg) and vice versa. Using carefully arranged actuators, the robot can be driven by the same set of motors in both wheeled mode (i.e., the wheel moves in 1-DOF rotational motion) and legged mode (i.e., the leg moves in 2-DOF planar motion), to enjoy the advantages of wheels on flat ground and employ the mobility of legs on rough terrain. It might be possible in the future to explore dynamic quadruped locomotion such as galloping [24]. To the best of our knowledge, this paper presents the first design and realization of four-leg/four-wheel transformable mobile robot.

Section II introduces the design concept of this robot, which is then followed by Section III that describes the leg–wheel transformation mechanism in detail. Section IV briefly outlines the robot mechatronics and software infrastructure. Section V introduces the robot development on the behavioral aspect, and Section VI reports on the experimental evaluation of the robot. Section VII concludes the paper.

II. Design Concept

The key component of this leg–wheel transformable robot is the "transformation mechanism" that is capable of deforming a specific portion of the body to act either as a wheel or a leg. This portion is hereafter referred to as "leg–wheel." From a geometric point of view, a wheel usually has a circular rim and a rotational axis located at the center of the rim. The rim contacts the ground, and the rotational axis connects to the body at a point hereafter referred to as a "hip" joint, as shown in Fig. 2(a). In general wheeled locomotion on flat ground, the wheel rotates continuously, and the ground-contact point of the wheel is located directly below the hip joint at a fixed distance (i.e., radius of the circular rim). On the other hand, in legged locomotion, the leg usually moves in a periodic manner, and there is no specific geometrical configuration between the hip joint and the ground-contact point; hence, their relative position varies frequently and periodically during locomotion. Based on this observation, shifting the hip joint out of the center of the circular rim and changing the continuous rotation motion to other motion patterns implies transforming of the locomotion from wheeled to legged mode. This inspired us to design a mechanism that is capable of directly controlling the relative position of the circular rim with respect to the hip joint, such that both wheeled and legged motions can be generated. Since the circular rim itself is a 2-D object, the straightforward method to achieve this goal is to add a second DOF that can adjust the relative position of the hip joint to the center of the circular rim along the radial direction. The motions of these two DOFs in this arrangement are also orthogonal to each other.

The mass and inertia of the leg as well as its given geometrical configuration strongly affect the functionality and agility of the legged motion. To decrease the inertia of the moving rim, the rim is supported by a single spoke, which also acts as the housing for the hip joint to slide within. To reduce the space taken by the rim, the rim is folded into half in the legged mode. Hereafter, it is referred to as the "half-circle leg," similar to the legs on the second generation of RHex in the sense of geometry. However, the compliant property is quite different: The legs of RHex are compliant, while those of this robot are rigid. Rim rigidity is important for wheeled locomotion, since a springy wheel may yield unsmooth locomotion. With active rotation of the circular rim and active translation along with the radial direction of the hip, the leg itself is equivalent to a 2-DOF system that has motions along two principal axes according to the polar coordinate in the sagittal plane depicted in Fig. 2(b). Compared to RHex with only one active rotational DOF per leg [19], the 2-DOF structure of the proposed system is more complicated but it greatly increases the freedom to adjust the robot posture and leg ground-contact timings, thereby providing the opportunity to explore different behavioral subspaces with fewer constraints.

The general four-wheel methodology of the wheeled platform is adopted in the robot design shown in Fig. 2(a), and the locomotion behavior of this robot is similar to that of four-wheel-drive vehicles. The distance between the hip joint and the rim is fixed at a value equal to the radius of the rim, and the active rotational DOF at the hip joint rotates the rim clockwise or counterclockwise, thus driving the robot forward or backward. The front wheels can be steered to achieve turning motion according to the Ackermann steering geometry shown in Fig. 2(c), where the centers of the radii of all the four wheels coincide at a single point C, the center of turning, on the extended line of the hind hip axis.

In legged mode, where the circular rims are folded in half and the hip joints are shifted close to the rims, the platform is transformed into a quadruped robot, as shown in Fig. 2(b). The length change of the leg is achieved by changing the position of the hip joint in the spoke, and swing of the leg is driven by the active rotational joint at the hip. The legged mode is designed for the robot to be capable of crossing various uneven surfaces, such as steps, bars, stairs, natural terrain, etc.

Note that all four leg–wheels are controlled individually; therefore, each leg–wheel can be independently operated in either wheeled or legged mode. However, the robot is currently set to operate exclusively in one mode or the other, since legs and wheels are advantageous in two distinct environments. When the robot moves on even surfaces, the wheeled mode is adopted since it can provide smooth, high-speed, and power-efficient locomotion. In contrast, when the robot moves on rough terrain, the legged mode is utilized for obstacle negotiation. If the leg–wheels are not used solely for locomotion but for some other tasks such as manipulation, a combination of the two may be desired.

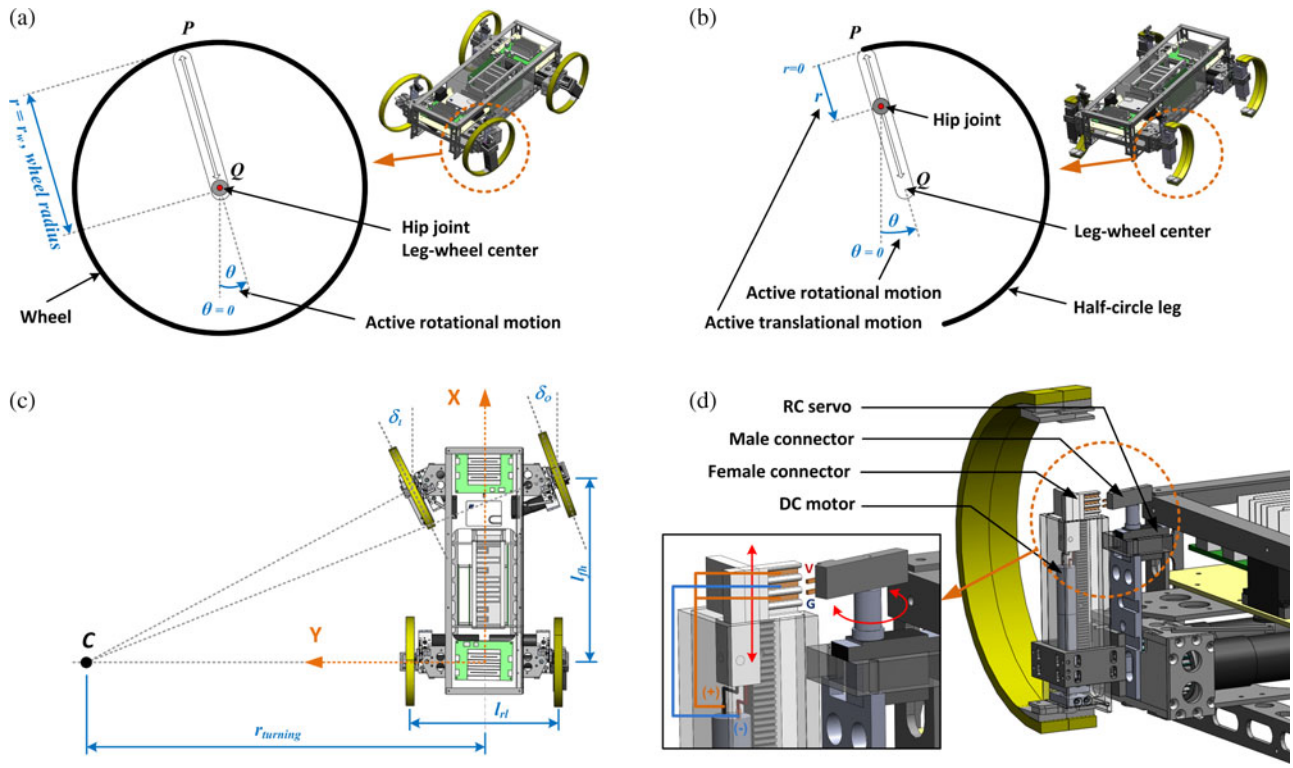

Fig. 2. Drawings of the robot: (a) detailed geometric illustration of the wheel, (b) detailed geometric illustration of the leg, (c) the Ackermann steering geometry, and (d) leg–wheel switching mechanism.

III. Leg–Wheel Transformation Mechanism

Switching between wheeled and legged modes of this transformable mobile robot is achieved by the transformation mechanism that includes a 2-DOF driving mechanism and a leg–wheel switching mechanism.

The 2-DOF driving mechanism provides two active motions on the leg–wheel component—rotation and translation of the spoke, with respect to the hip joint. If the hip joint is defined as the origin of the coordinate, the 2-DOF mechanism is indeed driving the spoke according to the polar coordinate. The rotational DOF of the spoke, which is equivalent to θ, is driven by the rotational motion of the square sleeve shown in Fig. 3(a), which is further driven by motor 1 with a belt transmission system comprising two pulleys and a timing belt without speed reduction. The rotation axis of the square sleeve is the axis of the hip joint. The translational DOF of the spoke, which is equivalent to r, is generated by the sliding motion between the spoke and the square sleeve. As shown in Fig. 3(b), the relative motion is provided by a rack–pinion mechanism, with the former fixed on the spoke and the latter mounted on the body and driven directly by motor 2. As a result, the kinematic mapping between the inputs (i.e., motor speeds $\dot{\boldsymbol{\varphi}}^T = [\dot{\varphi}_1 \quad \dot{\varphi}_2]^T$) and the outputs (i.e., leg motion $\dot{\boldsymbol{\theta}}^T = [\dot{r} \quad \dot{\theta}]^T$) can be derived as

$$\dot{\boldsymbol{\theta}} = \begin{bmatrix} \dot{r} \\ \dot{\theta} \end{bmatrix} = \begin{bmatrix} a & -a \\ 1 & 0 \end{bmatrix} \begin{bmatrix} \dot{\varphi}_1 \\ \dot{\varphi}_2 \end{bmatrix} = \boldsymbol{J}\dot{\boldsymbol{\varphi}} \tag{1}$$

where a, which is the radius of the pinion, determines the speed ratio from rotational to translational motion. The matrix relating the motor inputs $\dot{\boldsymbol{\varphi}}$ to the joint trajectories $\dot{\boldsymbol{\theta}}$, as shown in (1), is not singular; therefore, the inverse mapping can be uniquely derived. When the robot operates in wheeled mode, the hip joint must coincide with the center of the rim and the wheel radius should be fixed. Thus, according to (1), both motors

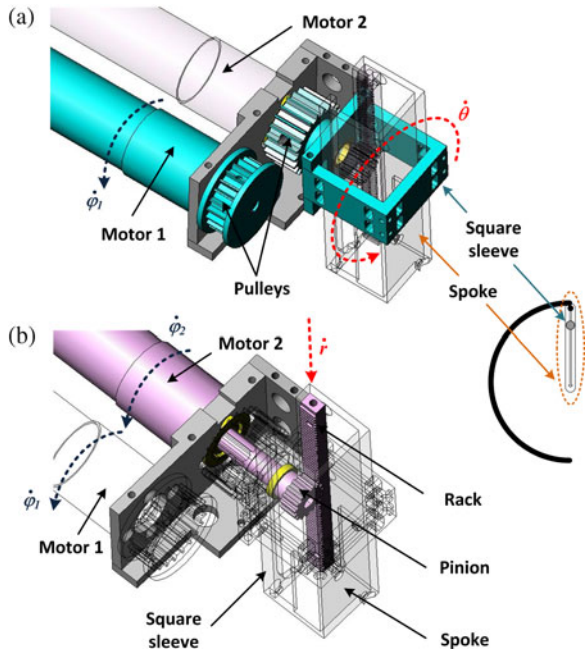

Fig. 3. Two-DOF driving mechanism: (a) rotational DOF and (b) translational DOF.

TABLE I
ROBOT SPECIFICATIONS

Length	Body	0.6 m
	Hip-to-hip	0.445 m
Width	Body	0.19 m
	Leg-to-leg	0.41 m
Height	Body	0.14 m
	Standing (wheeled mode)	0.195 m
	Standing (legged mode)	0.26 m
	Ground clearance (legged mode)	0.16 m
Leg-wheel (i.e., rim) diameter		0.215 m
Weight	Total	12.2 kg
	Body	8.27 kg
	Leg-wheel (each)	0.38 kg
	Battery	1.7 kg
Inertia	Leg	3.99×10^{-3} kg-m^2
	Wheel	5.23×10^{-3} kg-m^2
Actuator	Driving	60W DC motor (x8)
	Turning (wheeled mode)	RC servo (x2)
	Leg-wheel transformation	RC servo (x4)
		1W DC motor (x4)
Sensors	Encoder	(x8)
	Hall-effect	(x8)
	Temperature sensor	(x17)
	Battery current measurement	(x1)
	Battery voltage measurement	(x1)
	6-axis IMU	(x1)
	2-axis inclinometer	(x1)
	IR ranger	(x6)

are required to rotate at the same speed and direction, to yield $\dot{r} = a(\dot{\varphi}_1 - \dot{\varphi}_2) = 0$. Similarly, when the robot is operating in legged mode, because both $\dot{r}$ and $\dot{\theta}$ change frequently and periodically to create leg-like motion, both the motors are required to rotate as well. If the translational and rotational DOFs are independently driven by one motor each, then in wheeled mode, the motor for translational DOF should be operated in stall mode with no velocity. In this case, the motor draws a huge current and generates a significant amount of heat. In contrast, both motors used in the reported differential-drive-like mechanism are required to rotate, no matter the robot is operated in either wheeled or legged mode, which avoids stall-mode operation and potential problems of current overload and heat generation. In addition to the aforementioned feature, this design with motors on the body has two other advantages over the serial-link design:

1) It significantly reduces the weight and inertia of the leg, which further improves dynamic and control characteristics of the leg. The inertia of the leg–wheel in legged mode is even less than that in wheeled mode (i.e., 75%, as given in Table I).
2) It avoids the use of a slip ring to transmit power and control signals to the motor that drives the second link (i.e., r DOF).

The leg–wheel switching mechanism alters the shape of the circular rim. This rim consists of two half-circle rims: one is rigidly mounted on the spoke, and the other is connected to the output shaft of a small dc motor with a gearbox, which is installed inside the spoke, as shown in Fig. 2(d). By providing power to the dc motor, the latter rim can rotate with a range of 180° and switch the shape of the overall leg–wheel between one full-circle rim (wheeled mode) and two half-circle rims (legged mode). The gearbox is not back-drivable; therefore, the configuration of the movable rim can be adequately maintained even without power input to the motor. In contrast to using motor position control to maintain the leg–wheel configuration, this method is preferred since the dc motor is powered only during leg–wheel switching, reducing power consumption.

It is not feasible to drive the small dc motor by directly deploying a hard wire from the robot's body to the spoke since the leg–wheel may rotate continuously. Because physical space around the hip area is mostly taken up by the transmission mechanism, no space is left for installing a slip ring. Therefore, an RC servo and a connector pair, as shown in Fig. 2(d), are utilized. The female connector is rigidly mounted on the spoke, and the male connector, which is mounted on the top of the RC servo, is movable. When leg–wheel switching is performed, the male connector is rotated to connect the female connector, where power is transmitted from the robot body to the dc motor. In other robot operations, the male connector is set on the side, i.e., away from the workspace of the rotating spoke, to avoid collision. The direction in which the movable rim rotates (i.e., leg-to-wheel or wheel-to-leg switching) is determined by how the connectors connect to each other. As shown in Fig. 2(d), the female connector has three pins and the male connector has two pins. Positioning the spoke higher or lower with respect to the RC servo determines how either the upper or the lower two pins of the female connector contact the male connector, which further determines the rotation direction of the dc motor. This contact adjustment is easily achieved by utilizing the existing translational motion of the spoke (i.e., r DOF) without addition of extra motors. In our current design, leg–wheel switching is set to operate when the robot sits on the ground, so the rim of the leg–wheel is moved in the air without any heavy load applied to it. Thus, its motion can be actuated by a low-power and compact actuator with a simple time-based open-loop control.

IV. ROBOT INFRASTRUCTURE

The essential specifications are summarized in Table I. The main computation power on the robot is a 400-MHz real-time embedded control system (cRIO-9014, National Instruments) operating at a 1-kHz loop rate, together with a 3M gates field-programmable-gate-array (FPGA) embedded chassis (cRIO-9104) for high-speed signal exchange, such as a proportional–integral–derivative (PID) control for the dc motors, encoder readings, and pulsewidth modulation (PWM)-based RC servo commands. The microprocessor, running in a real-time operating system, communicates with the remote operator through an 802.11b wireless standard for high-level driving commands and robot health status. The FPGA directly connects to analog I/O (NI 9205 and NI 9264) and digital I/O (NI 9401 and NI 9403) modules, which further connect to various sensors and actuators on the robot.

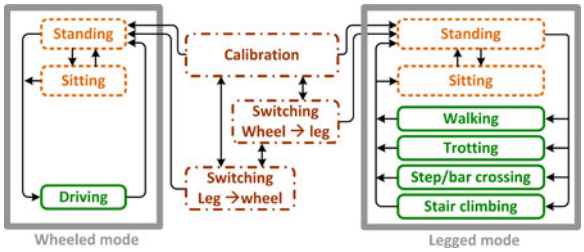

Fig. 4. Behaviors of the robot: text in dash-dotted brown, dashed orange, and solid green boxes indicate configuration setup, transient modes, and operation modes, respectively.

The robot is programmed with various state machines. Each state represents one particular operating behavior of the robot. The feasible behavior switching is shown in Fig. 4. Calibration is the procedure to find the absolute geometric configurations of two active DOFs on each leg–wheel with respect to the robot, which only needs to operate once immediately after the robot is powered on. Switching is the mode that changes the shape of the leg–wheel from wheel to leg and vice versa. The arrow indicates the possible modes that can be switched to and from the current mode. Currently, some mode transitions are automatic and some are done manually by a remote operator. For example, the robot can automatically switch to stair climbing gait or step/bar crossing gait when it confronts these environments. On the other hand, leg–wheel switching or walk–trot switching are done manually. The fully autonomous mode switching requires the robot to understand the environment at a recognition level. An accurate environment recognition system is under development.

V. Behavioral Development

For the robot moving in wheeled mode, trajectory planning of the two active DOFs on each hip is straightforward. Instead of using velocity control, the operation of wheeled mode in this robot requires accurate positioning of the leg–wheel configuration. Thus, position state is adopted as tracking target $\boldsymbol{\theta}^T(t) = [\, r(t) \quad \theta(t) \,]^T$. As shown in Fig. 2(a), $r\,(t)$ should remain at a value equal to the radius of the leg–wheel, and derivative of $\theta\,(t)$ directly determines the wheel's rotational speed. For forward and backward locomotion, $\theta\,(t)$s of all four wheels should be the same. For turning locomotion, the $\theta\,(t)$s of all the four wheels are no longer the same but their derivatives should be coordinated according to the Ackermann steering geometry

$$\cot\delta_i - \cot\delta_o = \frac{l_{\mathrm{rl}}}{l_{\mathrm{fh}}} \tag{2}$$

where δ_i and δ_o represent the turning angles of the inner and outer wheels, respectively, and l_{rl} and l_{fh}, respectively, represent the distances between the right–left and fore–hind wheels, as shown in Fig. 2(c). After determining the incremental change of $\boldsymbol{\theta}$, the joint trajectories $\boldsymbol{\varphi}^T(t) = [\,\varphi_1(t) \quad \varphi_2(t)\,]^T$ can then be calculated by integration of inverse mapping shown in (1).

For the robot moving in legged mode, the trajectory planning of $\boldsymbol{\theta}$ requires further development. Fig. 5(a) plots the leg's forward motion in the sagittal plane based on the assumption that no ground-contact slippage is happening. Because of the half-circle geometry, the motion of the leg on the ground is hybrid, where the leg performs rolling motion first, and then followed by motion with a fixed contact point. Thus, given a designated hip-to-ground-contact position vector $R_c = (c_x, c_z)$ with the hip's coordinates as the origin, the inverse mapping from the work space (i.e., vector R_c) to the joint space $\boldsymbol{\theta}$ has two cases. While the leg moves with a fixed contact point (i.e., $\theta > 0$), as shown in Fig. 5(b), the inverse mapping is straightforward

$$\begin{aligned} \theta &= \frac{\pi}{2} - a\tan 2(R_c) \\ r &= 2r_w - \|R_c\|_2 \end{aligned} \tag{3}$$

where r_w, $\|R\|_2$, $a\tan 2(R_c)$ represent the radius of the wheel, L_2 norm of vector R, and four-quadrant arctangent function, respectively. On the other hand, while the leg rolls on the ground (i.e, $\theta < 0$), the inverse mapping is given by

$$\begin{cases} \theta = \dfrac{\pi}{2} + \tan^{-1}\left(\dfrac{h_z - r_w}{h_x - o_x(\pi - \theta)}\right), & \text{if } h_z \neq r_w \\ \theta = \dfrac{o_x}{r_w}, & \text{if } h_z = r_w \end{cases} \tag{4}$$
$$r = \|R_w + R_h - R_o\|_2$$

where $\|R_w\|_2 = r_w$, $R_h = (h_x, h_z)$, $R_o = (o_x, r_w)$, and o_x denote the horizontal rolling distance from a designated configuration shown in Fig. 5(d). Note that R_h and R_o are position vectors starting from a specific leg configuration, as shown in Fig 5(a) and (d). Because of the involved trigonometric function, there is no straightforward analytical solution. Thus, the inverse kinematic in the real-time application is calculated based on the differential motions. Without loss of generality, assuming that the vectors $R_{h(i)}$ at time stamp i are known, the differential motion to the next time stamp $i+1$, as shown in Fig. 5(c), is

$$\begin{aligned} d\theta &= dR_h \sin(\pi/2 - \theta + \mu) \,/\, (\|R_c\|_2 \sin(\theta - \psi + \pi/2)) \\ dr &= dR_h \sin(\psi - \mu) \,/\, \sin(\theta - \psi + \pi/2). \end{aligned} \tag{5}$$

With the given initial condition, the leg configuration $\boldsymbol{\theta}$ in the rolling period can be continuously derived.

The 2-DOF driving mechanism of each leg provides the freedom to locate the hip joint (a hollow red dot) between the aerial phase (blue solid line) and stance phase (green solid line), as shown in Fig. 5(a). During the stance phase where the leg supports the body, intuitively planning the hip trajectory to move along with a horizontal line segment with fixed height h_z seems to yield the minimum alternation of body orientation, which further prevents energy from being consumed for periodic pose changes. During the aerial phase where the leg moves in the air to prepare for the next touchdown, assuming no leg dynamics involved, the hip trajectory is still a horizontal line segment because at that instant the body is supported by the other legs in stance phase.

The basic trajectory planning for walk and trot gaits are derived based on the rules described in the previous paragraph. In the stance phase, the motion along with the forward direction $x\,(t)$ is planned by a fifth-order polynomial with six given boundary conditions, including positions, velocities, and

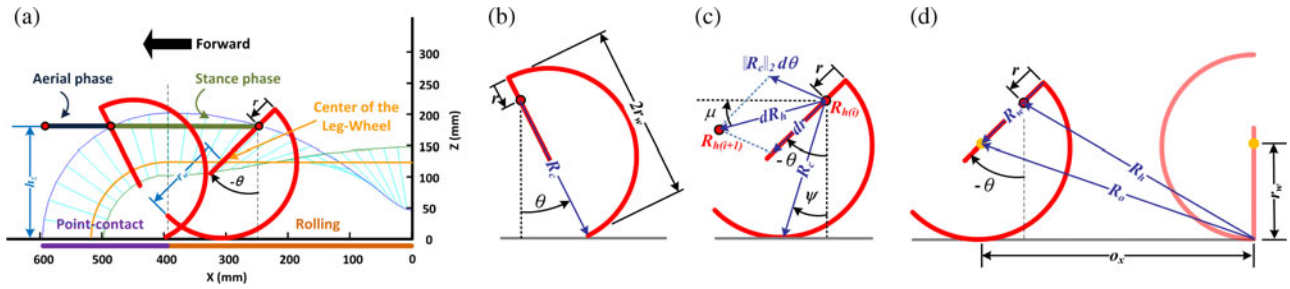

Fig. 5. Leg motion and kinematics: (a) hybrid motion of the half-circle leg on smooth ground, (b) point-contact motion, and (c), (d) rolling motion.

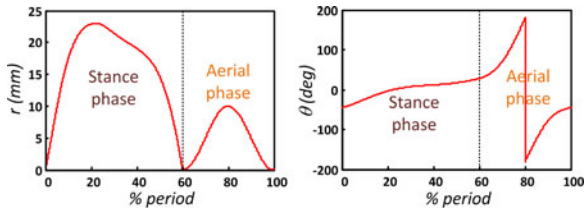

Fig. 6. Joint trajectories of the 2-DOF leg when the robot moves in a two-beat trot.

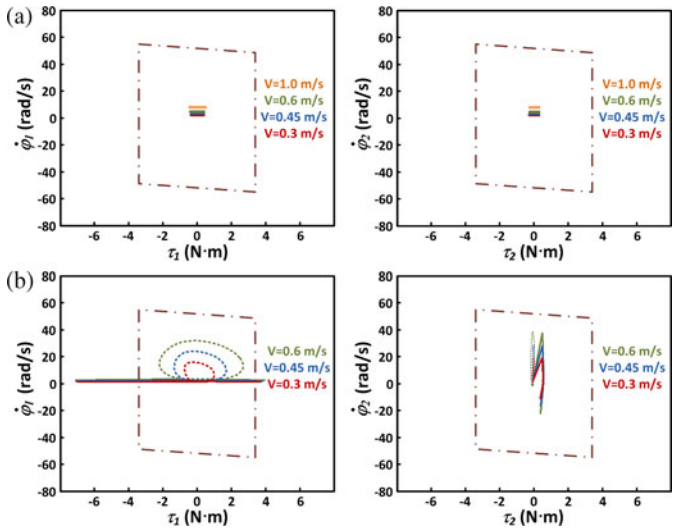

Fig. 7. Operation trajectories of motors when the robot operates with several forward velocities in the (a) wheeled mode and (b) legged mode. The dashed-dotted parallelograms represent the continuous operating zone of the motor.

accelerations of the initial and final positions of the stance phase. The motion in the vertical direction $z(t)$ is set constant, as described. The forward velocity is set constant as well. With designed $\mathbf{x}(t) = (x(t), z(t))$, the leg trajectories $\boldsymbol{\theta}(t)$ in the stance phase can then be calculated based on the inverse kinematics shown in (3) and (5). Because the leg trajectories in the aerial phase can be freely designed, they are directly planned in joint space $\boldsymbol{\theta}(t)$ to have a smooth transition from and to the stance phase without utilizing inverse kinematics. Fig. 6 shows joint trajectories when the robot moves in a typical two-beat trot, where the duty cycle of each leg is set at 60% and the two sets of diagonal legs have a 180° phase shift. On the other hand, the leg in typical four-beat walk gait has a 75% duty cycle and 90° phase shift implemented among the legs, so that the robot body is supported by three legs at every moment during locomotion. After the leg trajectories $\boldsymbol{\theta}(t)$ are determined, the joint trajectories $\boldsymbol{\varphi}(t)$ can then be calculated according to (1). One of the merits of legged locomotion is its ability to negotiate rough terrain. In contrast to most legged robots with a swing recovery phase, a robot utilizing full-turn rotating recovery can negotiate taller obstacles via normal walk or trot gaits. This strategy is bioinspired from observing a cockroach's step-crossing behavior, whereby it swings the front legs on top of an obstacle and lifts its body while crossing the obstacle [25], [26]. In addition, the tire treads mounted on the surface of the leg act like the spines on an animal's legs to latch onto small asperities (bumps or pits) on the surface [27], increasing traction. With these designs, the robot can cross a step or bar of various heights by simple open-loop control strategies.

The designed behavior should be investigated regardless of whether the associated joint trajectory can be generated by the empirical system. This evaluation requires the dynamic model of the robot. The Appendix briefly describes the mathematical relation of the motor supplying voltage to the body state of the robot. By importing the desired leg–wheel trajectories to (7)–(14), we are able to check whether the trajectories are within the working zone of the motors. To quantitatively and fairly compare the dynamic characteristics of the robot locomotion in the wheeled and legged modes, the developed trajectories shown in the previous paragraphs are imported into equations for evaluation, and the robot in both modes is set to have the same forward velocity and to fix its center of mass (COM) vertical height during locomotion. Fig. 7(a) and (b) shows the operation trajectories of the motors while the robot, respectively, operates in wheeled and legged modes with several preset forward velocities. The dashed-dotted parallelogram represents the motor continuous operation zone with given nominal voltages (i.e., equal to the voltage of the battery) [28]. In the wheeled case shown in Fig. 7(a), although the forward velocity of the robot is set constant, the offset COM of the leg–wheel results in the variation of motor torques spanning in both positive and negative works. This happens even though the motors are generally in low load since the operation trajectories are far from the boundary. In the legged case, the motors in contrast are under a much heavier load than in the wheeled case. The solid and dotted curves represent the operation trajectories while the leg is in stance phase and then in aerial phase. As shown in Fig. 6, the aerial phase uses less than half the time of the stance phase, but the spanning angle is around five times that of the stance

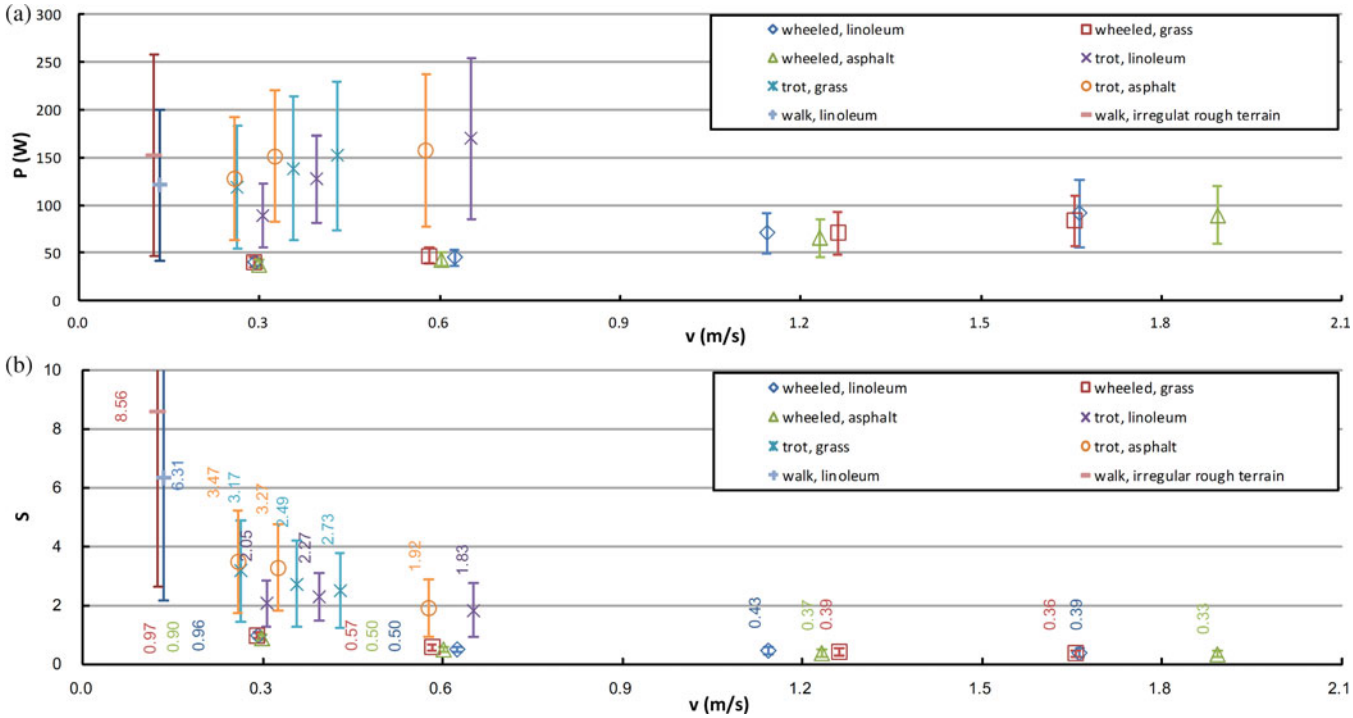

Fig. 8. Plots of (a) power and (b) specific resistance versus forward speed of the robot operated in various scenarios.

phase. Therefore, the required motor speeds and torques are much more dramatic than those in the stance phase. When the preset forward velocity of the robot is $V = 0.6\,\mathrm{m/s}$, the motors may operate slightly over the maximum achievable condition in a short duration. When this happens, PD control may yield larger error. Even though, the simulation suggests that the preset leg trajectories are feasible since almost all the trajectories are in the rhombus zone. Note that the dynamic models shown in (7)–(14) do not include the mechanical transmission loss. In addition, the trajectory control also requires extra torque available for regulation. Thus, we empirically found that the speed $V = 0.6\,\mathrm{m/s}$ is the maximum achievable speed of the robot in legged mode under current trajectory design. More detailed results are reported in Section VI. Fig. 7 also reveals that the operation trajectories of both motors in wheeled mode are similar. In contrast, in legged mode, motor 1 has more dramatic load than that of motor 2, which further indicates that the required torque (τ_h) is the dominant factor and the effect of the radial force (f_h) variation is unimportant. This is mainly due to the fact that the lengths of moment arms in these two axes are significantly different, where the detailed description is reported in Section VI.

VI. Performance Evaluation and Discussion

Wheeled locomotion and legged locomotion have significantly different characteristics. In the former, interaction with the ground is smooth and continuous. In contrast, legged locomotion is generally varying and intermittent. In contrast to most of the hybrid robots that extend the original leg and wheel functions in a mixed manner, our paper tries to maintain the original advantages of legs and wheels by incorporating both the functions in one robot. Furthermore, by utilizing the same power source and transmission system, this platform provides an unusual opportunity to explore the output variation with the same inputs. Due to the unique infrastructure in which both the modes exist on the same robot, our performance evaluation not only addresses the advantages of each mode but also compares the underlying physical principles between them. The widely utilized criteria for locomotion such as power, speed, power efficiency, motion smoothness, and terrain negotiation capability are adopted for evaluation. A collection of robot behavioral movies is available at http://ieeexplore.ieee.org.

The power efficiency is evaluated according to the widely used measure, "specific resistance" [29], which was determined by weight of the robot *mg*, its averaged power consumption P, and its averaged forward speed v

$$S = \frac{P}{mgv}. \tag{6}$$

The power consumption recorded here was the total power consumed from the battery, not the mechanical power produced by the motors. Thus, this measurement can provide an important run time of the robot with the given battery capacity.

Fig. 8(a) and (b) plots the power and specific resistance versus the measured forward speed of the robot operating on three different surfaces (linoleum, asphalt, and grass) and at various speed settings (wheeled modes: 0.3, 0.6, 1.2, and 1.8 m/s, equivalent to 0.5, 1, 2, and 3 body lengths per second; legged trot gait: three different preset leg motion periods 1.3, 1.1, and 0.9 s). The statistically summarized means and standard are presented, where each datum is the average of instant measurements from at least three experimental runs. The power consumed by the computation and peripheral electronics is around 15–20 W

(independent of operation mode). Overall power consumption is mainly determined by the behavior of motor operation. Several conclusions can be derived as follows:

1) The robot operating in legged mode (80–160 W) generally consumes more power than in wheeled mode (40–80 W) since varying and intermittent force interaction of the robot leg with the ground consumes more energy in the position-based trajectory planning. Due to the same reason, the standard deviations of the power measurements in the former case have larger variations as well.
2) The commercial motors prefer high-speed and low-load rotary motion in a fixed direction. Thus, when the robot operates in wheeled mode, the motor torque can effectively and continuously contribute to the locomotion via fast and efficient rolling behavior since the rolling of the wheel also implies the continuous rotation of the motors, as described in Section V and shown in (1). In contrast, the legged motion usually requires a low-frequency and high-torque swing motion where the motor accelerates/decelerates frequently and operates in a wide speed range. This phenomenon is revealed by the motion model developed in Section V and observed in Fig. 7. As a result, experimentally we found that achievable leg stride frequency ($\sim$1.2 Hz) is indeed less than the achievable wheel rolling frequency ($\sim$2.3 Hz). In addition, the body forward distance per period in legged mode is around 1/3–1/4 of that in wheeled mode. As a result, although the leg length is almost twice the wheel radius, the forward speed in legged mode is around 1/4–1/2 of that in wheeled mode.
3) Because faster motor motion usually gives the robot a higher forward speed, the power consumption increases as forward speed increases. The increasing trend in speed is more dramatic than in power; therefore, the specific resistance decreases as the speed increases. This trend indicates that the robot, as currently designed, is more energy-efficient in high-speed locomotion. The specific resistance drops to averaged 0.3 when the robot operates in wheeled mode and moves at three body lengths per second. The specific resistance in legged mode hovers around 2–3.5, comparable to the performance of the reported legged robot [30], [31].
4) Effect of the ground types on power consumption is insignificant since the standard deviations of the tests on different terrains are considerably larger than the difference of the means, especially when the robot is operated in legged mode. For the same trajectory setting, the robot yields a different forward velocity due to different contact friction, and the speed variation of the robot on different ground types increases with the increase in speed.
5) The robot operating in a walk gait on flat linoleum was also evaluated for performance comparison, although that gait is specifically designed for crossing rough terrain. Although four-leg coordination is quite different in the walk and trot gaits, the individual leg trajectory tracking is similar as described in Section V; therefore, the power consumptions of these two gaits are roughly similar. However, since the high duty cycle yields a more stable but slower motion, the specific resistance of the walk gait is higher than that of the trot gait. The phenomenon is similar to four-legged animals, which switch their gait from walk to trot for power efficiency when their forward speed increases [32].

TABLE II
AVERAGED MOTION ACCELERATION OF THE ROBOT OPERATED IN VARIOUS SCENARIOS (UNIT: m/s^2)

	Speed setting	linoleum	asphalt	grass
Wheeled	0.3 (m/s)	0.41(0.21)	0.57(0.17)	0.51(0.22)
	0.6 (m/s)	0.40(0.16)	0.58(0.21)	0.69(0.24)
	1.2 (m/s)	1.67(0.93)	1.71(0.83)	1.65(0.74)
	1.8 (m/s)	2.36(1.07)	1.72(0.85)	2.59(0.99)
Legged	Slow	2.72(1.46)	4.11(2.78)	4.01(2.33)
	Medium	4.33(2.42)	4.98(3.12)	5.58(3.68)
	High	5.22(2.94)	4.81(2.57)	5.38(3.14)

TABLE III
AVERAGED TRACKING ERRORS OF THE ROBOT OPERATED IN WHEELED MODE

	Speed setting	linoleum	asphalt	grass
θ error (deg)	0.3	1.05(0.23)	0.93(0.23)	1.26(0.26)
	0.6	1.80(0.18)	1.74(0.28)	2.04(0.31)
	1.2	3.59(0.43)	3.35(0.49)	3.61(0.55)
	1.8	5.23(0.48)	4.87(0.62)	5.22(0.71)
r error (mm)	0.3	0.046(0.029)	0.041(0.028)	0.057(0.029)
	0.6	0.036(0.018)	0.043(0.031)	0.056(0.032)
	1.2	0.085(0.048)	0.082(0.042)	0.083(0.047)
	1.8	0.066(0.044)	0.053(0.040)	0.077(0.052)

Motion smoothness is characterized by body state measurements from inertial measurement unit (IMU). Similarly, the robot operates on the same three different surfaces and at the same speed settings. Table II lists the timed-average L_2 norm (vector sum) of three-axis body state component results. Gravity-induced acceleration was compensated; therefore, only motion acceleration was accounted for. As expected, locomotion of the robot in wheeled mode on linoleum and asphalt is smoother than on the slightly rough grass surface, while in legged mode, it has a more dramatic variation because of the wider range of force interaction with the ground. When the forward speed is faster, the motion is bumpier as well.

Table III lists the trajectory tracking performance of the robot in wheeled mode, which is judged by averaged tracking errors of four 2-DOF driving modules. The robot's locomotion on grass is bumpy and slippery due to its uneven and soft nature. This phenomenon leads to wider variation and uneven distribution of ground-contact forces to four wheels/legs, which further results in larger tracking errors when comparing these two values to those from locomotion on the other two types of surfaces. In contrast, the asphalt has the largest friction coefficient among all three surfaces, so the driving force can be transmitted smoothly and equally from the ground, to the four wheels, then to the body, which, in general, leads to small tracking errors. The table also reveals the characteristics of the coupled two DOFs. Although the output DOFs are driven by the same two equal-power motors

TABLE IV
PERCENTAGE ERROR OF TURNING RADIUS OF THE ROBOT OPERATED IN WHEELED MODE

	Speed setting	linoleum	asphalt	grass
R=1.25m	0.3	9.4(4.4)	7.2(9.5)	15.7(4.0)
	0.6	8.7(3.7)	7.4(6.2)	16.8(5.6)
	1.2	9.4(1.1)	8.6(6.7)	16.0(2.4)
	1.8	11.4(2.5)	8.7(6.6)	19.0(8.7)
R=1.5m	0.3	5.4(2.0)	3.5(3.0)	11.4(4.2)
	0.6	7.3(1.8)	3.6(2.4)	11.4(3.7)
	1.2	5.7(1.2)	4.1(3.3)	11.4(3.7)
	1.8	6.6(2.0)	5.8(5.3)	15.7(2.4)
R=1.75m	0.3	5.5(2.5)	2.6(2.2)	10.2(1.3)
	0.6	5.5(2.5)	0.3(2.5)	11.2(5.4)
	1.2	5.0(1.8)	2.0(3.7)	12.7(4.6)
	1.8	6.1(3.1)	1.3(7.7)	12.9(8.6)

with kinetic mapping shown in (1), the tracking performance in r is better than that in θ for the following reasons:

1) The lengths of the moment arm of these two DOFs are significantly different—wheel radius for θ DOF and pinion gear radius for r DOF (i.e., 125:8), and the motion with longer moment arm has less resistance to the end force.
2) The error of the r-DOF is periodic and varied between positive and negative values while the wheel is rolling. In contrast, the error of the θ-DOF is cumulative during forward locomotion. Thus, the tracking error of parameter θ has an apparent increase while the forward speed of the robot increases, during which more dynamics are involved and more traction torque is required. The results confirm the characteristics of the differential drive mechanism.

The robot's turning locomotion in wheeled mode was evaluated. The robot was driven and turned with three different designated turning radii $R = 1.25$ m (minimum turning radius), 1.5 m, and 1.75 m on the same three surfaces, and four preset forward speeds. Because the actual forward speed is coupled with turning radius and angular velocity, the preset forward velocity is adopted as the comparison basis. Because the tracking condition of individual wheels is similar in forward and turning motion, performance of power and specific resistance in turning motions is similar to that in forward motion, which yields that speed is a crucial factor, not the ground surface. For the same reason, the performance is not a function of turning radius. This further indicates that while the robot in wheeled mode moves freely on the flat ground, the speed is the sole factor affecting power and specific resistance. Table IV lists the statistical results of the percentage error of turning radius in these tests. The percentage errors of the robot's motion on the linoleum and asphalt surfaces are less than 10%, which indicates that the Ackermann steering controlled by the RC servos has adequate performance. The asphalt surface with large friction yields small error. In contrast, the slippery and soft grass has the least resistance to the centrifugal effect, so the percentage error is the largest. For a given turning radius, the percentage error doesn't have a clear increase with the increase of forward velocity, so it is not induced by the side slip of the wheels due to the centrifugal force, but by the accuracy of the Ackermann turning control. Since turning control is more sensitive when the robot turns with a small radius, the percentage error increases with the decrease of the turning radius.

Fig. 9. Robot operated in various scenarios: (a) step crossing, (b) bar crossing, (c) natural rough terrain walking, and (d) stair climbing.

For legged movement, besides the flat terrain test described earlier, the evaluation concentrated on the mobility of the robot over uneven terrains, including step and bar crossing, walking over natural irregular terrain, and climbing stairs, as shown in Fig. 9. The original movies are available at http://ieeexplore.ieee.org. The trajectories for step and bar crossing are empirically generated with preset trajectories and tracked by PD position control. The high-level gait transition between walking/trotting and step/bar crossing is automatic if an obstacle is observed or cleared. The generation of stair climbing trajectory requires certain planning, and the primitive result has been reported in [33]. Similarly, no extra sensory feedback is required. As for natural rough terrain walking, the gait is just an ordinary walking gait, as reported in Section V, where at least three legs are set down at any instant to provide basic walking stability.

Fig. 9(a) plots the typical scene of the robot climbing the step. The performance is evaluated based on the results from ten experimental runs, and the rate of successful passing is adopted as the quantitative measure. The robot in legged mode can cross a 24.5-cm-high step (i.e., 1.25 times the leg length and around 150% of the ground clearance) with about a 70% success rate, but with no success on the 25-cm-high step. In comparison, the robot in wheeled mode can only cross a 7.1-cm-high step nearly 100% of the time, but with no success on the 7.9-cm-high step. Sharp declines in the success rate with a slight increase in height indicate that: 1) the successful rate is dominated by the relative geometry between the robot and the obstacle, and 2) the possible performance variation due to the dynamic effect is insignificant. When the height of the step increases to a certain value, the legs cannot pull the COM of the body past the edge of the step and reliably position the body on the step. As a result, the robot slides down, unable to climb the step.

Fig. 9(b) plots the typical scene of the robot climbing the bar. The robot in legged mode can pass over a 22-cm-high step with about an 80% success rate, but with no success on the 24.3-cm-high step. The robot in wheeled mode can overcome a 4.9-cm-high step with 100% success, but no success on the 6.7-cm-high step. Similarly, the robot in legged mode has a much better climbing ability than in wheeled mode. In addition, the robot climbs better over a step than a bar. In the former case, the forelegs (front wheels) have continuous ground contact force to pull the body after they encounter the top of the step. But in crossing the bar, contact between the forelegs (front wheels) and the bar happens only briefly, and it is lost before the body's COM passes the edge of the bar. Thus, the shift of the robot's

COM can be done only by propulsion of the hind legs. Without assistance from the forelegs, the height of the bar that the robot can cross is less than that of the step.

Fig. 9(c) plots the typical scene of the robot walking over a natural environment full of tree roots. The height variation of the surface is random. Empirical evaluation confirmed that though the simple open-loop walk gait of the robot was not capable of surface adaption to yield smooth locomotion, the naïve three-point ground contact strategy and sequential full-rotation leg motion in the current gait did endow the robot with the capability to successfully negotiate the irregular terrain. In addition, the power consumption and specific resistance of the robot walking on the flat and irregular terrains are also plotted in Fig. 8. For the same parameter sets of the walk gait, the robot walking on the irregular terrain consumes 50% more power than on the flat linoleum surface. Since the speed doesn't alter much, the specific resistance also increases 50%.

Fig. 9(d) plots a typical example of the robot climbing stairs [33]. With the open-loop design of the gait, the robot can successfully climb stairs with a width between 25 and 30 cm and height within 150–170 cm. However, because the stair size varies from step to step, the configuration error may be accumulative and the performance not reliable. A revised algorithm that can perform online trajectory generation to adapt to a wider configuration range of stairs is required to make the behavior more reliable.

In summary, this section reports on various experimental results with *Quattroped*, mainly on the locomotion ability within its wheeled and legged modes. Legs and wheels have their advantages in two distinct environments. The existing hybrid robots are indeed designed to balance performance of the robot in both environments within one single platform. Based on different design strategies and target applications, each robot has its own advantages and disadvantages. From aspects of either morphology or control strategy, the hexapod Whegs series is very close to a wheeled vehicle. By removing the "rim" of the wheel, Whegs indeed significantly increases rough terrain negotiability, while retaining wheel-like speed. For example, it can move at a speed of three body lengths per second and cross barriers of about 1.5 times the leg length [17]. However, maybe due to its compact size, no stair climbing behavior has been reported. The quadruped Loper has a similar wheeled-style leg morphology and open-loop control strategy but with a different body size and number of legs. It can move at 1.8 body lengths per second and can climb stairs [11]. The hexapod RHex and the quadruped Scott use the same morphology of 1 DOF per leg, but utilize more leg-like legs with compliant characteristics for investigating dynamic legged locomotion. With an intrinsically stable tripod gait and half-circle leg, RHex can cross bars/steps of 1.25 times the leg length, move over natural rough terrain, and climb ordinary stairs [19], [34]. Its reported quantitative performance of the earlier behaviors is similar to that of *Quattroped* reported here. Due to the simple 1-DOF design per leg of the aforementioned robots, the ability of legged maneuvering is limited, while the robot's body state during locomotion is strongly determined by the environment. The 2 DOFs per leg in *Quattroped* provide body posture adjustability and, more importantly, offer the possibility of changing configuration to wheeled locomotion, which significantly increases the power efficiency and motion smoothness that the earlier robots cannot achieve. The successor of Scott, the quadruped PAW, also has 2 DOFs per leg by adding an active wheel at the distal end of the compliant leg [8]. Wheeled motion can achieve four body lengths per second with specific resistance of 0.14, better than *Quattroped* can achieve. Because the DOF for leg maneuvering remains the same, its ability to negotiate rough terrain, though not reported, is expected to be similar to that of Scott. The quadruped Roller Walker has 3 DOFs per leg and can adjust its body posture more actively and stably than the robots shown earlier. In addition, with a passive wheel at the distal end of the leg, the robot in the roller-walk mode can move at a speed of 0.5–2 body lengths per second with a specific resistance of 0.5–1.2, much faster and more power efficient than its original crawl gait. It has a speed of 0.02–0.2 body lengths per second with a specific resistance of 5–10 [31]. Perhaps due to indirect driving of the wheels, the performance of power efficiency in roller-walk mode is slightly less than that of Scott and *Quattroped* in wheeled mode. Note that hybrid robots in general have more DOFs than ordinary wheeled vehicles, and most likely, these robots in wheeled mode still require controlling all DOFs. Therefore, the power efficiency of the former platforms is still less than that of the latter.

VII. Conclusion

We reported on the design and performance evaluation of a novel leg–wheel transformable robot named *Quattroped.* The robot is equipped with a transformation mechanism capable of directly changing the morphology of its wheels into 2-DOF legs, where the same set of actuators can be efficiently utilized in both modes. It follows that the robot can act as either a four-wheel-drive vehicle (wheeled mode) or as a quadruped (legged mode). The design concept, especially the transformation mechanism, is described in detail. Through the design of a 2-DOF differential driving module, motor power can be effectively utilized in both modes. The robot infrastructure, including the structure, mechatronics, and software infrastructure, is briefly described. Based on the developed mechanical components and mechatronics, various behaviors are developed based on straightforward trajectory generation methods. Together with the developed dynamic model of the robot, the robot behavior and motor working status can be analyzed. The behavioral performance of the robot in both wheeled and legged modes is experimentally evaluated. As expected, the robot in wheeled mode yields a smoother ride and better power efficiency. On the other hand, the robot in legged mode has better mobility to cross obstacles or rough terrain. Combining both wheeled and legged features on the same robot truly provides a better adaption to the environment.

On the hardware side, we are implementing various sensors such as GPS, vision, and a laser ranger to improve the robot's perception ability. On the behavioral side, we are developing legged behaviors with closed-loop features to improve the robot's mobility on other challenging terrains and to explore the robot's behaviors in the dynamic region. With perception

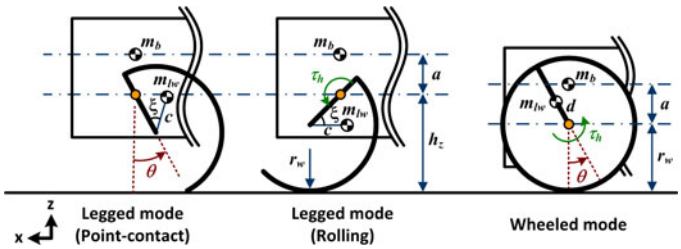

Fig. 10. Notations for dynamic model development.

capability and a bank of behaviors for different terrains, the robot may in the future perform automatic behavior switching.

APPENDIX

LEG–WHEEL DYNAMIC CHARACTERISTICS

Although physically the leg–wheel is one component, its form (i.e., wheeled or legged) significantly determines the robot's locomotion behavior. Because the leg–wheel utilizes the same set of motors and mechatronic system (i.e., same inputs), it is important to understand performance differences between these two modes. For the purpose of comparison, the robot's sagittal-plane locomotion on flat ground is adopted for dynamic model formulation and quantitative analysis, since this is the nominal domain of wheeled operation. Thus, body pitch and roll variations are ignored. Mechanical damping is also ignored. Ground contact is assumed within static friction, yielding pure rolling or fixed-point contact.

Fig. 10 shows several notations for model formulation. The symbols m and I denote mass and inertia, respectively, x and z, respectively, denote forward and vertical displacements, ω denotes angular velocity, and subscripts b and lw represent body and leg–wheel, respectively. The COM of the body is located above the hip joint with vertical distance a. The COM of the leg–wheel in legged mode is parameterized in polar coordinates (c, ξ) with distance c to the leg–wheel center and angle ξ with respect to the spoke. In the wheeled mode, the COM is on the spoke and with distance $d = c\cos\xi$ to the center. Because the materials utilized for the rim of the wheel are identical for the whole rim, the moment of inertia of the leg–wheel with respect to the center $I_{\mathrm{lw}c}$ remains the same in both wheeled and legged modes. Thus, the relative distance of the leg to the center of the rim remains the same. The moment of inertia with respect to the COM I_{lw} in either wheeled or legged mode can then be derived according to the parallel-axis theorem.

When the robot is operated in wheeled mode, $r(t)$ is controlled to be the same as the radius of the wheel r_w. By the Lagrangian method, the dynamics equation of the overall robot can be written as

$$\tau_h = \left(\frac{m_b r_w^2}{4} + m_{lw}\left(r_w^2 + d^2 + 2r_w d\cos\theta\right) + I_{lw}\right)\ddot{\theta} - m_{lw} d\sin\theta g - m_{lw} r_w d\sin\theta\dot{\theta}^2 \tag{7}$$

$$f_h = \frac{m_b(-r_w\sin\theta\ddot{\theta} - \cos\theta g)}{4} \tag{8}$$

where τ_h and f_h, respectively, represent hip torque and hip force in the radial direction, and g is the gravity constant. Because of the leg–wheel's offset COM (i.e., existence of d), other wheel dynamic terms such as gravity and centrifugal effect [i.e., the second and third terms on the right-hand side of (7)] generate modulating torque effects on the system dynamics. By subtracting these terms from the hip torque τ_h, the resultant torque divided by the resultant robot inertia [i.e., coefficient of the first term on the right-hand left side of (7)] yields the wheel acceleration $\ddot{\theta}$, which is linearly proportional to the body forward acceleration $\ddot{x}_b$. Equation (8) shows the dynamics of the hip force acting in the radial direction. Although $r(t) = r_w$ does not change in the wheeled mode, the hip force f_h still varies and depends on the configuration of the leg–wheel to balance the forward acceleration and gravity.

When the robot is operating in legged mode, two types of locomotion exist: rolling motion and motion with a fixed ground-contact point, as described in Section V. For the former case, the dynamics equation of the robot with a two-beat trot gait can be derived as

$$\begin{aligned}\Bigg(&\frac{m_b\left(r_w^2 + (r_w - r)^2 + 2r_w(r_w - r)\cos\theta\right)}{2} \\ &+ m_{lw}\left(r_w^2 + c^2 + 2r_w c\cos(\theta - \xi)\right) + I_{lw}\Bigg)\ddot{\theta} = \tau_h \\ &+ \left(\frac{m_b(r_w(r_w - r)\sin\theta)}{2} + m_{lw}(r_w c\sin(\theta - \xi))\right)\dot{\theta}^2 \\ &+ m_b\left((r_w - r) + r_w\cos\theta\right)\dot{r}\dot{\theta} + \frac{m_b r_w\sin\theta\ddot{r}}{2} \\ &+ \left(\frac{m_b((r_w - r)\sin\theta)}{2} + m_{lw} c\sin(\theta - \xi)\right) g\end{aligned} \tag{9}$$

$$f_h = \frac{m_b(\ddot{r} - r_w\sin\theta\ddot{\theta} + (r_w - r)\dot{\theta}^2 - \cos\theta g)}{2}. \tag{10}$$

For the second case, the dynamics equation can be written as

$$\begin{aligned}&\left(\frac{m_b(2r_w - r)^2}{2} + m_{lw}(r_w + c)^2 + I_{lw}\right)\ddot{\theta} = \tau_h \\ &+ m_b(2r_w - r)\dot{r}\dot{\theta} + \Bigg(\frac{m_b((2r_w - r)\sin\theta)}{2} \\ &+ m_{lw}(r_w\sin\theta + c\sin(\theta - \xi))\Bigg) g\end{aligned} \tag{11}$$

$$f_h = \frac{m_b\left(\ddot{r} + (2r_w - r)\dot{\theta}^2 - \cos\theta g\right)}{2}. \tag{12}$$

In the legged mode, $(r(t), \theta(t))$ are functions of time and all their derivatives can be derived based on (5). As expected, (9)–(12) contain various dynamic terms such as gravity and centrifugal effect. Since the distance between the COM of the leg–wheel and the hip varies during locomotion, the terms are coupled in a more complicate manner than those shown in (7) and (8).

The hip torque τ_h and hip force f_h are provided by the motor torques through the 2-DOF driving mechanism shown in Fig. 3. The force mapping can be derived according to the principle of virtual work,

$$\boldsymbol{F} = \begin{bmatrix} f_h \\ \tau_h \end{bmatrix} = \left(\boldsymbol{J}^T\right)^{-1} \boldsymbol{\tau} = \begin{bmatrix} 0 & -1/a \\ 1 & 1 \end{bmatrix} \begin{bmatrix} \tau_1 \\ \tau_2 \end{bmatrix}. \quad (13)$$

Equation (13) indicates that the hip torque τ_h is determined by the sum of motor torques and the hip force is simply determined by motor 2 torque τ_2, with division by the radius of the pinion gear a. The coupling in (13) is complementary to that in (1).

The torque of dc brushed motor can further be represented as a function of supplying voltage V and its speed $\dot{\varphi}$

$$\tau = \frac{K_T V}{R} - \frac{K_T K_e \dot{\varphi}}{R} \quad (14)$$

where K_T, K_e, and R are torque constant, voltage constant, and terminal resistance, respectively. As a result, the hip torque τ_h and hip force f_h can be further represented as functions of supplying voltage, motor 1 speed $\dot{\varphi}_1$, and motor 2 speed $\dot{\varphi}_2$. Note that the motor inductance is ignored in (14) since it is comparably small.

The overall system dynamics can be evaluated by the combination of (7)–(14). More specifically, with a given nominal motor voltage V, the motor torques behave according to (14), and then the hip torque and hip force further behave according to (13). Together with the dynamic equations shown in (7)–(12), body state of the robot can be derived and simulated.

ACKNOWLEDGMENT

The authors would like to thank National Instruments' Taiwan Branch for their kind support of this study through equipment and technical consulting.

REFERENCES

[1] P. Liljeback, K. Y. Pettersen, O. Stavdahl, and J. T. Gravdahl, "Snake robot locomotion in environments with obstacles," *IEEE/ASME Trans. Mechatronics*, vol. 17, no. 6, pp. 1158–1169, Dec. 2012.

[2] N. O. Perez-Arancibia, J. P. Whitney, and R. J. Wood, "Lift force control of flapping-wing microrobots using adaptive feedforward schemes," *IEEE/ASME Trans. Mechatron.*, vol. 18, no. 1, pp. 155–168, Feb. 2013.

[3] S. Lohmeier, T. Buschmann, and H. Ulbrich, "System design and control of anthropomorphic walking robot LOLA," *IEEE/ASME Trans. Mechatron.*, vol. 14, no. 6, pp. 658–666, Dec. 2009.

[4] Y. D. Hong and J. H. Kim, "3-D command state-based modifiable bipedal walking on uneven terrain," *IEEE/ASME Trans. Mechatron.*, vol. 18, no. 2, pp. 657–663, Apr. 2013.

[5] D. J. Braun, J. E. Mitchell, and M. Goldfarb, "Actuated dynamic walking in a seven-link biped robot," *IEEE/ASME Trans. Mechatron.*, vol. 17, no. 1, pp. 147–156, Feb. 2012.

[6] F. Michaud, D. Létourneau, M. Arsenault, Y. Bergeron, R. Cadrin, F. Gagnon, M.-A. Legault, M. Millette, J.-F. Parè, M.-C. Tremblay, P. Lepage, Y. Morin, J. Bisson, and S. Caron, "Multi-modal locomotion robotic platform using leg-track-wheel articulations," *Auton. Robots*, vol. 18, pp. 137–156, 2005.

[7] S. Hirose, "Variable constraint mechanism and its application for design of mobile robots," *Int. J. Robot. Res.*, vol. 19, pp. 1126–1138, 2000.

[8] J. A. Smith, I. Sharf, and M. Trentini, "PAW: A hybrid wheeled-leg robot," in *Proc. IEEE Int. Conf. Robot. Autom.*, 2006, pp. 4043–4048.

[9] Y. Takita, N. Shimoi, and H. Date, "Development of a wheeled mobile robot 'octal wheel' realized climbing up and doen stairs," in *Proc. IEEE/RSJ Int. Conf. Intell. Robots Syst.*, 2004, pp. 2440–2445.

[10] N. Shiroma, Y.-H. Chiu, Z. Min, I. Kawabuchi, and F. Matsuno, "Development and control of a high maneuverability wheeled robot with variable-structure functionality," in *Proc. IEEE/RSJ Int. Conf. Intell. Robots Syst.*, 2006, pp. 4000–4005.

[11] S. D. Herbert, A. Drenner, and N. Papanikolopoulos, "Loper: A quadruped-hybrid stair climbing robot," in *Proc. IEEE Int. Conf. Robot. Autom.*, 2008, pp. 799–804.

[12] G. Quaglia, D. Maffiodo, W. Franco, S. Appendino, and R. Oderio, "The Epi.q-1 hybrid mobile robot," *Int. J. Robot. Res.*, vol. 29, pp. 81–91, 2010.

[13] T. Estier, Y. Crausaz, B. Merminod, M. Lauria, R. Piguet, and R. Siegwart, "An innovative space rover with extended climbing abilities," in *Proc. Robotics 2000*, pp. 333–339.

[14] C. Grand, F. Benamar, F. Plumet, and P. Bidaud, "Stability and traction optimization of a reconfigurable wheel-legged robot," *Int. J. Robot. Res.*, vol. 23, pp. 1041–1058, 2004.

[15] S. Nakajima, E. Nakano, and T. Takahashi, "Motion control technique for practical use of a leg–wheel robot on unknown outdoor rough terrains," in *Proc. IEEE/RSJ Int. Conf. Intell. Robots Syst.*, 2004, pp. 1353–1358.

[16] M. Lacagnina, G. Muscato, and R. Sinatra, "Kinematics, dynamics and control of a hybrid robot Wheeleg," *Robot. Auton. Syst.*, vol. 45, pp. 161–180, 2003.

[17] R. T. Schroer, M. J. Boggess, R. J. Bachmann, R. D. Quinn, and R. E. Ritzmann, "Comparing cockroach and Whegs robot body motions," in *Proc. IEEE Int. Conf. Robot. Autom.*, 2004, pp. 3288–3293.

[18] J. B. Jeans and D. Hong, "IMPASS: Intelligent mobility platform with active spoke system," in *Proc. IEEE Int. Conf. Robot. Autom.*, 2009, pp. 1605–1606.

[19] U. Saranli, M. Buehler, and D. E. Koditschek, "RHex: A simple and highly mobile hexapod robot," *Int. J. Robot. Res.*, vol. 20, pp. 616–631, 2001.

[20] C. C. Phipps, B. E. Shores, and M. A. Minor, "Design and quasi-static locomotion analysis of the rolling disk biped hybrid robot," *IEEE Trans. Robot.*, vol. 24, no. 6, pp. 1302–1314, Dec. 2008.

[21] R. Tadakuma, A. Maruyama, E. Rohmer, K. Nagatani, Y. Kazuya, M. Aigo, M. Shimojo, M. Higashimori, and M. Kaneko, "Mechanical design of the wheel-leg hybrid mobile robot to realize a large wheel diameter," in *Proc. IEEE/RSJ Int. Conf. Intell. Robots Syst.*, 2010, pp. 3358–3365.

[22] T. Okada, W. T. Botelho, and T. Shimizu, "Motion analysis with experimental verification of the hybrid robot PEOPLER-II for reversible switch between walk and roll on demand," *Int. J. Robot. Res.*, vol. 29, pp. 1199–1221, 2010.

[23] T. Seo and M. Sitti, "Tank-like module-based climbing robot using passive compliant joints," *IEEE/ASME Trans. Mechatron.*, vol. 18, no. 1, pp. 397–408, Feb. 2012.

[24] W. Hu, D. Marhefka, and D. E. Orin, "Hybrid kinematic and dynamic simulation of running machines," *IEEE Trans. Robot.*, vol. 21, no. 3, pp. 490–497, Jun. 2005.

[25] J. T. Watson, R. E. Ritzmann, S. N. Zill, and A. J. Pollack, "Control of obstacle climbing in the cockroach, Blaberus discoidalis. I. Kinematics," *J. Comparative Physiol. A, Neuroethol. Sensory Neural Behav. Physiol.*, vol. 188, pp. 39–53, Feb. 2002.

[26] Y.-C. Chou, W.-S. Yu, K.-J. Huang, and P.-C. Lin, "Bio-inspired step-climbing in a hexapod robot," *Bioinspiration Biomimetics*, vol. 7, 036008, pp. 1–19, 2012.

[27] J. C. Spagna, D. I. Goldman, P. Lin, D. E. Koditschek, and R. J. Full, "Distributed mechanical feedback in arthropods and robots simplifies control of rapid running on challenging terrain," *Bioinspiration Biomimetics*, vol. 2, pp. 9–18, 2007.

[28] M. Lasa and M. Buehler, "Dynamic compliant quadruped walking," in *Proc. IEEE Int. Conf. Robot. Autom.*, 2001, pp. 3153–3158.

[29] G. Gabrielli and T. H. von Karman, "What price speed?" *ASME Mech. Eng.*, vol. 72, pp. 775–781, 1950.

[30] P. Gregorio, M. Ahmadi, and M. Buehler, "Design, control, and energetics of an electrically actuated legged robot," *IEEE Trans. Syst., Man, Cybern. B, Cybern.*, vol. 27, no. 4, pp. 626–634, Aug. 1997.

[31] G. Endo and S. Hirose, "Study on roller walker: Energy efficiency of roller walk," in *Proc. IEEE Int. Conf. Robot. Autom.*, 2011, pp. 5050–5055.

[32] N. C. Heglund, C. R. Taylor, and T. A. McMahon, "Scaling stride frequency and gait to animal size—Mice to horses," *Science*, vol. 186, pp. 1112–1113, 1974.

[33] S. C. Chen, K. J. Huang, C. H. Li, and P. C. Lin, "Trajectory planning for stair climbing in the leg–wheel hybrid mobile robot Quattroped," in *Proc. IEEE Int. Conf. Robot. Autom.*, 2011, pp. 1229–1234.

[34] E. Z. Moore, D. Campbell, F. Grimminger, and M. Buehler, "Reliable stair climbing in the simple hexapod 'RHex'," in *Proc. IEEE Int. Conf. Robot. Autom.*, 2002, pp. 2222–2227.

Shen-Chiang Chen received the B.S. and M.S. degrees in mechanical engineering from National Taiwan University, Taipei, Taiwan, in 2009 and 2011, respectively.

He is currently a Teaching Assistant in the Department of Mechanical Engineering, National Taiwan University. His current research interests include mechanism design, robot dynamics and control, and mobile robots applications.

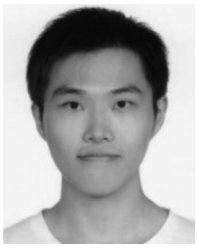

Ke-Jung Huang received the B.S. and M.S. degrees in mechanical engineering from National Taiwan University, Taipei, Taiwan, in 2010 and 2012, respectively.

He is currently in military service in Taiwan. His current research interests include computer programming, modeling, and robot dynamics and control.

Wei-Hsi Chen received the B.S. degree in 2011 in mechanical engineering from National Taiwan University, Taipei, Taiwan, where he is currently working toward the M.S. degree.

His current research interests include bioinspired robotics, mechanism design, and robot dynamics and control.

Shuan-Yu Shen received the B.S. degree in mechanical engineering from National Central University, Taoyuan, Taiwan, in 2007, and the M.S. degree in mechanical engineering from National Taiwan University, Taipei, Taiwan, in 2009.

He is currently a Manager at Yu-Long Motorcycle Parts Manufacturing Company Ltd., Taoyuan. His current research interests include mechanism design, robot dynamics and control, and sensor applications.

Cheng-Hsin Li received the B.S. and M.S. degrees in mechanical engineering from National Taiwan University, Taipei, Taiwan, in 2008 and 2010, respectively.

He is currently an Electronic Engineer at FEGO Precision Industrial Company, Tai-Chung, Taiwan. His current research interests include robot dynamics and control and mobile robot applications.

Pei-Chun Lin (S'02–M'05) received the B.S. and M.S. degrees in mechanical engineering from National Taiwan University (NTU), Taipei, Taiwan, in 1996 and 1998, respectively, and the M.S. degree in electrical engineering and computer science and the Ph.D. degree in mechanical engineering from the University of Michigan, Ann Arbor, MI, USA, both in 2005.

From 2005 to 2007, he was a Postdoctoral Research Fellow in the Department of Materials Science and Engineering, University of Pennsylvania, Philadelphia, PA, USA. He is currently an Associate Professor in the Department of Mechanical Engineering, NTU. His current research interests include bioinspired robotics, mechanical design, sensor design/fusion, control, dynamic locomotion, and compliant composites.